Chemistry Europe
European Chemical Societies Publishing

WILEY VCH

Excellence in Chemistry Research

Announcing our new flagship journal

- Gold Open Access
- Publishing charges waived
- Preprints welcome
- Edited by active scientists

Meet the Editors of *ChemistryEurope*

Luisa De Cola
Università degli Studi di Milano Statale, Italy

Ive Hermans
University of Wisconsin-Madison, USA

Ken Tanaka
Tokyo Institute of Technology, Japan

Check for updates

Batteries & Supercaps

Research Article
doi.org/10.1002/batt.202300291

Chemistry Europe
European Chemical Societies Publishing

www.batteries-supercaps.org

Special Collection

Challenges and Opportunities for Large-Scale Electrode Processing for Sodium-Ion and Lithium-Ion Battery

Julian Klemens,*[a] Ann-Kathrin Wurba,[b] David Burger,[a] Marcus Müller,[c] Werner Bauer,[c] Sebastian Büchele,[c] Olatz Leonet,[d] J. Alberto Blázquez,[d] Iker Boyano,[d] Elixabete Ayerbe,[d] Helmut Ehrenberg,[c] Jürgen Fleischer,[b] Anna Smith,[c] Philip Scharfer,[a] and Wilhelm Schabel[a]

Sodium-ion batteries are an emerging technology that is still at an early stage of development. The electrode processing for anode and cathode is expected to be similar to lithium-ion batteries (drop-in technology), yet a detailed comparison is not published. There are ongoing questions about the influence of the active materials on processing parameters such as slurry viscosity, coating thicknesses, drying times, and behavior during fast drying. Herein, the expected drying time for the same areal capacity of anodes (graphite vs. hard carbon) and cathodes (lithium iron phosphate vs. Prussian blue analogs) are compared based on respective specific capacities reported in the literature. Estimates are made for the materials' impact on production speed or dryer length. Within the experimental part, water-based slurries of the same composition are mixed using different active materials according to identical procedure and the viscosity is compared. When drying at a constant drying rate (0.75 $g\,m^{-2}\,s^{-1}$), lithium iron phosphate electrodes with different areal capacities (1–3 $mAh\,cm^{-2}$) are shown to have the highest adhesion. For high drying rates (3 $g\,m^{-2}\,s^{-1}$) at constant areal capacity, especially the investigated electrodes based on hard carbon show that no binder migration occurs.

Introduction

Nowadays, the lithium-ion battery (LIB) is the state-of-the-art battery technology and is considered the benchmark for many fast-growing applications, such as mobile and stationary energy storage. However, current LIB technology is facing substantial challenges with respect to safety, sustainability, cost, and especially raw material supply risks. While most of today's R&D is concentrated on LIB related systems, shifting to novel battery chemistries besides LIB may open effective ways to overcome such challenges. Sodium-ion batteries (SIB) constitute a paradigmatic example of such promising, alternative non-Li energy storage system, following pioneering efforts and breakthroughs from world-wide research teams.[1]

SIB components' materials are abundant and easily accessible. Much larger worldwide Na resources (2.36% of the earth's crust is sodium, compared to 0.0017% for lithium),[2] being free of the necessity to use critical raw materials (CRM) such as cobalt or graphite and the use of an aluminum current collector for both electrodes promise a cost reduction and reduce supply risks.[3] In addition, SIB function with a similar working principle as LIB[4–7] and SIB production is considered as a drop-in technology in terms of manufacturing protocols and equipment as those required for LIB.[8] Therefore, the incentive for battery manufacturers to switch to new battery technologies, such as SIB is going to come down to the final cost per kWh and the carbon footprint under forthcoming local legislation.[9] But, although the first-generation commercial SIB products have already entered the energy storage market[8] (e.g., Contemporary Amperex Technology Co. Ltd, Faradion, TIAMAT), aiming for light mobility and stationary applications, SIB still are only in a preliminary stage. Despite the environmental, economic, and long-term performance advantages, SIB cell production has not established itself on the market yet. One reason may be that the manufacturability and the electrode processing for different material systems or particle morphologies are poorly understood,[10–14] posing a greater risk for investment in large-scale production than for established LIB systems. Focusing mostly on lab-scale applications it is not clear from the literature which challenges or opportunities are associated by

[a] J. Klemens, D. Burger, Dr.-Ing. P. Scharfer, Prof. Dr.-Ing. W. Schabel
Thin Film Technology (TFT)
Karlsruhe Institute of Technology (KIT)
Straße am Forum 7, 76131 Karlsruhe (Germany)
E-mail: julian.klemens@kit.edu

[b] A.-K. Wurba, Prof. Dr.-Ing. J. Fleischer
Institute of Production Science (wbk)
Karlsruhe Institute of Technology (KIT)
Kaiserstr. 12, 76131 Karlsruhe (Germany)

[c] Dr. M. Müller, Dr. W. Bauer, S. Büchele, Prof. Dr. H. Ehrenberg, Dr. A. Smith
Institute for Applied Materials (IAM)
Karlsruhe Institute of Technology (KIT)
Hermann-von-Helmholtz-Platz 1, 76344 Eggenstein-Leopoldshafen (Germany)

[d] O. Leonet, Dr. J. A. Blázquez, Dr. I. Boyano, Dr. E. Ayerbe
CIDETEC, Basque Research and Technology Alliance (BRTA)
P° Miramón 196, 20014 Donostia-San Sebastián (Spain)

Special Collection This publication is part of a joint Special Collection dedicated to Post-Lithium Storage, featuring contributions published in Advanced Energy Materials, Batteries & Supercaps, and ChemSusChem.

© 2023 The Authors. Batteries & Supercaps published by Wiley-VCH GmbH. This is an open access article under the terms of the Creative Commons Attribution License, which permits use, distribution and reproduction in any medium, provided the original work is properly cited.

© 2023 The Authors. Batteries & Supercaps published by Wiley-VCH GmbH

changing from LIB to SIB. More specifically, electrode production conditions for SIB vs. LIB are mainly unknown. The constraints related to the production capacities and the challenges that arise when the active material is changed from LIB to SIB are to be discussed. This study compares materials that are currently considered promising and are intended to cover the capacity range to be a LIB substitute and show that parts of the current global infrastructure investments in LIB cell production could be used for SIB production as well.

Anode active material

Graphite (Gr) is commonly chosen as the primary active material for anodes in LIB. Nevertheless, it is unsuitable for SIB due to sodium's limited ability to intercalate into Gr, resulting in significantly reduced capacities.[15] As a result, amorphous carbon materials, and predominantly hard carbon (HC), are typically preferred as an anode in SIB, owing to their cost-effectiveness and electrochemical performance.[16] HC is seen as the current benchmark material for SIB regarding energy density[17] and is primarily produced by the pyrolysis of biomass[18–20] or synthetic organic materials. The inability of these precursors to graphitize is attributed to their high oxygen content and disordered structure. HC retains its disordered structure alongside randomly oriented pseudo graphitic domains, which exhibit larger interlayer spacing compared to graphitic carbon. This unique characteristic allows the intercalation of Na^+ ions. HC also contains micro and mesopores, as well as residual heteroatoms (such as N, S, P, B, etc.), which provide additional storage sites for sodium and pathways for rapid Na^+ ion transport. To develop suitable HC for SIB, it is necessary to tune relevant properties, such as interlayer spacing, pore structure, and the presence of defects and heteroatoms. However, a comprehensive understanding of the mechanisms involved in Na^+ ion storage (which is still a topic of discussion)[21] is crucial to design successful strategies for the production of engineered HC.[2]

The primary challenge for HC is enhancing its storage capacity and reducing the irreversible capacity loss in the first de-sodiation step, to equal or surpass the capacity of Gr in LIB, which reaches 372 $mAh\,g^{-1}$. Currently, practically measured capacities for HC, typically evaluated in coin cells against metallic sodium, range from 200 to 450 $mAh\,g^{-1}$.[1] The majority of reported values in literature tend to average around 300 $mAh\,g^{-1}$.[22]

Cathode active material

Lithium layered transition metal oxides ($LiTMO_2$) are some of the most successful cathode materials for commercial LIB. Similarly, Na_xTMO_2 are of particular interest for SIB due to their high specific capacity, a variety of redox-active elements, and the possibility for manufacturers to employ already established synthesis processes from the LIB industry. Nevertheless, sodium layered oxides encounter significant hurdles such as irreversible phase changes during cycling, limited air stability, complex charge-compensation mechanisms, and comparatively high cost for the complete cell when compared to $LiFePO_4$-based LIB cells.[23]

Alternative promising cathode active materials of SIB are polyanionic compounds and Prussian blue analogs (PBA).[24] Polyanion-type materials exhibit high operating potentials due to the inductive effect of polyanion groups. Their robust 3D-framework significantly decreases the structural variations during the de/intercalation of sodium ions. Moreover, the effect of strong X–O (X = S, P, Si, etc.) covalent bonds can effectively inhibit the release of oxygen. These advantages contribute to the superior cycle stability and high safety of polyanion-type materials. Among polyanionic compounds, vanadium (V)-based polyanionic compounds have tended to receive more attention in recent years due to their many advantages (cycle stability, high voltage).[25–27] Many V-based polyanionic compounds exhibit a high operating voltage of over 3.4 V (vs. Na^+/Na) owing to the inductive effect of polyanionic groups and V redox.[25] However, their low electronic conductivity and limited capacity still restrict a further application.

PBA have garnered significant interest in the field of SIB due to their cost-effectiveness, easy synthesis, high working potentials, high theoretical capacity, and low toxicity.[28] The general chemical formula for PBA can be expressed as $A_xM'[M(CN)_6]_{1-y}z\cdot H_2O$, where A_x is an alkaline metal and M & M' are transition metal cations.

Electrode processing and microstructure formation

One of the costliest steps in roll-to-roll electrode manufacturing is the drying of the applied slurry (investment and energy consumption). Cell costs can be significantly reduced by increasing the throughput and shortening the length of the dryer.[29] In this context, the drying time is a decisive production factor for the analysis of the production speed and the required dryer length. Reported electrode production (coating and drying) speeds for LIB are in the range of 25–50 $m\,min^{-1}$[30] or higher (~80 $m\,min^{-1}$).[31,32] High coating speeds of 50 $m\,min^{-1}$ have been proven to be possible for high quality electrode coatings (coating edge quality without coating defects) for intermittent coating.[33] In principle, high production speeds are associated with longer dryer length (at the same drying rate) and, thus, related to higher investment costs. The literature notes that the extension of the dryer presents an increased need for control of process parameters and web tension.[30] However, drying in electrode manufacturing and post drying[34,35] currently still form bottlenecks that prevent an increase of throughput for the entire electrode production, which makes it necessary to reduce drying times. There is no need to extend the dryer length if the drying rate after coating could be increased to reduce drying times and increase production rates. However, for most standard LIB electrodes, faster drying can result in the depletion of binder in the vicinity of the current collector and accumulation on the top of the electrode in the direction of the separator.[10–12,36–38] This

© 2023 The Authors. Batteries & Supercaps published by Wiley-VCH GmbH

25666223, 2023, 11, Downloaded from https://chemistry-europe.onlinelibrary.wiley.com/doi/10.1002/batt.202300291 by Cochrane Germany, Wiley Online Library on [20/12/2023]. See the Terms and Conditions (https://onlinelibrary.wiley.com/terms-and-conditions) on Wiley Online Library for rules of use; OA articles are governed by the applicable Creative Commons License

undesired migration results in a decrease of adhesion and possibly leads to delamination of the electrode coating from the current collector.[10,39–42] In parallel the inhomogeneous distribution of binder and conductive additives after fast drying causes decreases in cell performance due to the increase in electrical and ionic resistances.[11,12,42–44] Binder migration occurs during the microstructure formation of slurry-based electrodes. After the application of the wet coating, the solvent evaporates, and the microstructure of the porous electrode network is formed. At the beginning of the drying process, the solvent content corresponds to the initial solvent content of the slurry. The evaporation of the solvent starts right after coating and the film shrinks according to the adjusted drying rate until the final dry-film thickness of the electrode is reached. At this point, the particle system has formed a dense network (porous microstructure) with the final porosity still filled with solvent. The solvent-filled pores empty by capillary transport. In this emptying mechanism of a pore network with a pore radius distribution, larger pores empty first, and smaller pores, filled to the surface with solvent, remain filled and sucking solvent from the larger pores towards the surface. Due to the randomly distributed and still filled small pores on the surface of the microstructure, the drying rate remains constant even during capillary transport of the binder. This effect is known for many porous material systems.[45–48] The binder (and possibly conductive additive) is transported by advection through the structure. With that process the concentration of binder near the current collector decreases and near the separator side increases,[12] resulting in a loss of adhesion and higher ionic resistance.[10,11,49,50] It is shown in literature that the adhesion force and the migration of the binder are closely interrelated and the adhesion force is an indirect measure for the homogeneity of the binder distribution at increasing drying rate.[12,41,43] In addition, it is reported in the literature that the loss of adhesion and, thus, a decrease of contacting with the current collector results in an increase of electrical resistivity.[12,36,50–52] Electrical pathways could be cut further by a movement of the conductive additive during capillary transport. However, this is only shown for higher areal loadings.[52]

One way to increase the drying rate without causing deterioration of the electrode properties is to use small particles. For HC and Gr it is known that by using smaller particles, binder migration can be reduced or completely prevented.[10,13] This effect is probably caused by a better fixation of the carboxymethyl cellulose (CMC) and styrene-butadiene rubber (SBR) elements with smaller particles. In addition, it was shown for HC electrodes that up to very high drying rates (10 s drying time, ~2.3 $mAh\,cm^{-2}$, 300 $mAh\,g^{-1}$) there is no negative influence on the adhesion force and also the ionic resistance does not increase, indicating the parallelism of the property development of adhesion and electrochemical performance with increasing drying rate.[10]

Another option to increase the drying rate significantly without a change in adhesion force is the use of, for example, NIR drying[39] or multi-stage drying profiles for industrial drying.[43] Regarding the comparison of very different active materials in this study, it is to be noted that except for Gr electrodes with the one-component binder polyvinylidene fluoride (PVDF) and the solvent N-methyl-2-pyrrolidone (NMP),[43] it is not known how different electrode compositions, binder systems, porosities, or active materials would affect the design of a multi-stage drying profile.

Electrodes' bending stiffness

In industrial manufacturing the dry electrodes are further processed in roll-to-roll processes including many winding operations.[30] During calendering some electrodes become brittle depending on the materials and compaction rate.[53] The electrode separator composite (ESC) is formed by stacking, folding and winding operations, depending on the cell format. During these manufacturing processes the electrodes undergo mechanical stress.[54] Sufficient coating adhesion and mechanically stable electrodes are required to avoid scrap. To gain more insights into the mechanical stability of electrodes, Gupta et al.[55] performed U-shaped, two-point bending tests on single-sided coated NMC cathodes to investigate their bending stiffness. The coating of the samples was subjected to tension when the substrate was inside and to compression when the coating was inside. Using this method, they determined the elastic tensile and bulk moduli of the coating to understand the expansion and contraction of the active material particles during cycling. Schilling et al.[54] developed a test rig to investigate the bending forces that occur during winding processes for the cell assembly. The electrode is moved over a predetermined radius while a force is applied. They evaluated their experiments in terms of surface changes and contact resistance and suggest minimum winding radii.

In this article, the expected drying time and electrode properties for a switch in electrode production from corresponding LIB to SIB electrodes for anodes (Gr vs. HC) and cathodes (LFP vs. PBA) are analyzed. In order to be competitive, the production speeds of SIB electrodes should not be lower than those of LIB electrodes. Specific capacities from the literature are used as a basis for a realistic comparison. Since the SIB materials used have a lower capacity, an increase in loading or production speed is required to achieve comparable production capacities to LIB. Hence, the drying time is calculated for different areal capacity and drying rates. The drying rate is used as a universal parameter, which is transferable consistently between lab-, pilot- and industrial scale electrode drying.[45] The production speed for a given dryer length and the dryer length for a given production speed is compared for all materials. The experimental section of the paper compares the water-based processing of anodes and cathodes. The viscosity at identical composition and identical mixing parameters gives information about the relation between slurry and particle properties. The adhesion and microstructure formation are characterized by increasing areal capacity (1, 2, 3 $mAh\,cm^{-2}$) and for different drying rates (0.75, 1.5, 3 $g\,m^{-2}\,s^{-1}$) at a fixed areal capacity of 2 $mAh\,cm^{-2}$ to investigate the effect of binder migration. In addition, the electrodes' bending stiffness is investigated for increasing areal

© 2023 The Authors. Batteries & Supercaps published by Wiley-VCH GmbH

25666223, 2023, 11, Downloaded from https://chemistry-europe.onlinelibrary.wiley.com/doi/10.1002/batt.202300291 by Cochrane Germany, Wiley Online Library on [20/12/2023]. See the Terms and Conditions (https://onlinelibrary.wiley.com/terms-and-conditions) on Wiley Online Library for rules of use; OA articles are governed by the applicable Creative Commons License

Research Article
doi.org/10.1002/batt.202300291
Chemistry Europe
European Chemical Societies Publishing

capacity for all materials, to be able to estimate the challenges in the further processing of the electrodes.

Results and Discussion

Drying time, production speed, dryer length

For the comparison of LIB vs. SIB regarding electrode processing and manufacturing parameters, anodes (Gr vs. HC) and cathodes (LFP vs. PBA) are used. Figure 1 shows scanning electron microscopy (SEM) images of the particles used for slurry preparation and drying experiments.

The LIB and SIB anode and cathode active materials differ in particle morphology and size, which is discussed in more detail in the next sections about the processing.

For comparison of the calculated areal mass loading, drying time and production speed, literature values for the specific capacities of the materials are used to give more practical data for the comparison (Table 1).[23]

For the chosen SIB anodes and cathodes, the capacity is higher for LIB materials, which has an influence on the manufacturing parameters. The areal mass loading (m_{area}/g m^{-2}) is calculated according to Equation (1)

$$m_{area} = \frac{c_{area}}{q\ x_{active}} \quad (1)$$

with the areal capacity (c_{area}/mAh cm^{-2}) divided by the specific capacity (q/mAh g^{-1}) of the active material and the share of the active material (x_{active}/kg kg$_{solid}^{-1}$). For all materials an active material content in the dry electrode of 93 wt-% is used in this study. Based on the areal mass loading and an assumed solid content of 43 wt-% the areal mass loading of the solvent m_s (g m^{-2}) can be calculated [Equation (2)].

$$m_S = m_{area}\ X \quad (2)$$

The solvent loading X (g$_{solvent}$ g$_{dry\ electrode}^{-1}$) is obtained from the conversion of the solvent content. The drying time is calculated according to Equation (3)

$$t = \frac{m_S}{\dot{m}_s} \quad (3)$$

from the areal mass loading of the solvent $m_{solvent}$ (g m^{-2}) divided by the drying rate $\dot{m}_s$ (g m^{-2} s^{-1}). More information about the drying rate is given in the Experimental Section.

Figure 2(left) shows the areal mass loading and the drying time for a constant drying rate of 1.5 g m^{-2} s^{-1} (considered as industrially relevant drying rate)[30,39] as function of the areal capacity for all materials. Figure 2(right) shows the relationship of the drying time from the drying rate for 2 mAh cm^{-2} electrodes for the materials used.

Figure 2(left) shows that due to the difference in the specific capacity of the materials, the areal mass loading for cathodes is higher than for anodes. With increasing areal capacity, the absolute difference in areal mass loading between LIB and SIB materials increases for both anode and cathode, which has an impact on the drying time. It can be deducted that for the comparison in this study the drying time of LIB and SIB battery slurries with the same solid content and share of active material is especially depending on the capacity of the material. For each of the materials, it can be seen that an increase in areal capacity leads to an equivalent increase in drying time. With their lower capacity, the drying time at the same areal capacity is increased for SIB materials. For a given production line, the difference in drying times due to the capacity of the materials results in different production speeds for anodes and cathodes but especially for LIB and SIB materials. For similar drying times between LIB and SIB, the drying rate must be increased. As the connection between drying time, dryer length and process speed is not straight forward Figure 2(right) shows the drying time as a function of increasing drying rate. With increasing drying rate, the drying time can be significantly reduced. It can be seen that the difference between the drying times of anodes and cathodes for LIB and SIB becomes less for higher drying rates. For the same areal capacity of 2 mAh cm^{-2}, the drying time difference between the anodes (Gr to HC) is 5 s and between the cathodes 6 s for a drying rate of 3 g m^{-2} s^{-1}. It is to be noted that for a production line with a fixed dryer length,

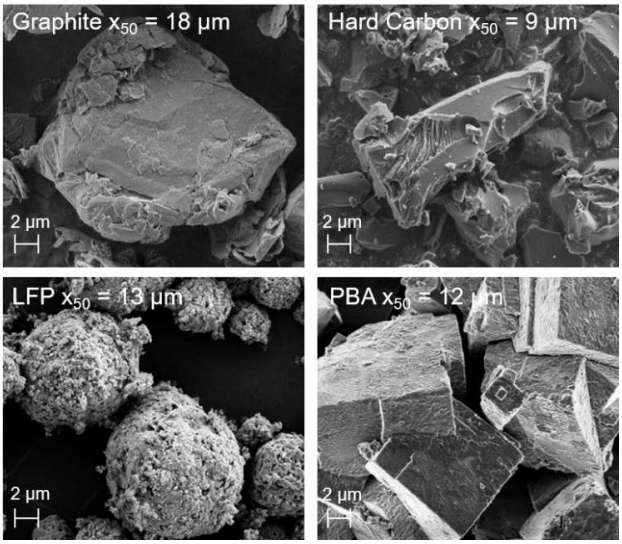

Figure 1. SEM of Gr, HC, LFP, and PBA powder and the average particle diameter x_{50} determined by laser diffraction. The average particle diameter of Gr is about two-times higher than for HC. LFP and PBA show almost the same measured average particle diameter. Although it should be noted that all particles are especially different in their particle morphology.

Table 1. Overview of the specific capacities considered from the literature for the calculation of the areal mass loading and drying time of anode and cathode materials for LIB and SIB.[10,22,23]

	LFP	PBA	Gr	HC
Spec. capacity [mAh g^{-1}]	165	149	360	300

© 2023 The Authors. Batteries & Supercaps published by Wiley-VCH GmbH

25666223, 2023, 11, Downloaded from https://chemistry-europe.onlinelibrary.wiley.com/doi/10.1002/batt.202300291 by Cochrane Germany, Wiley Online Library on [20/12/2023]. See the Terms and Conditions (https://onlinelibrary.wiley.com/terms-and-conditions) on Wiley Online Library for rules of use; OA articles are governed by the applicable Creative Commons License

Research Article
doi.org/10.1002/batt.202300291
Chemistry Europe
European Chemical Societies Publishing

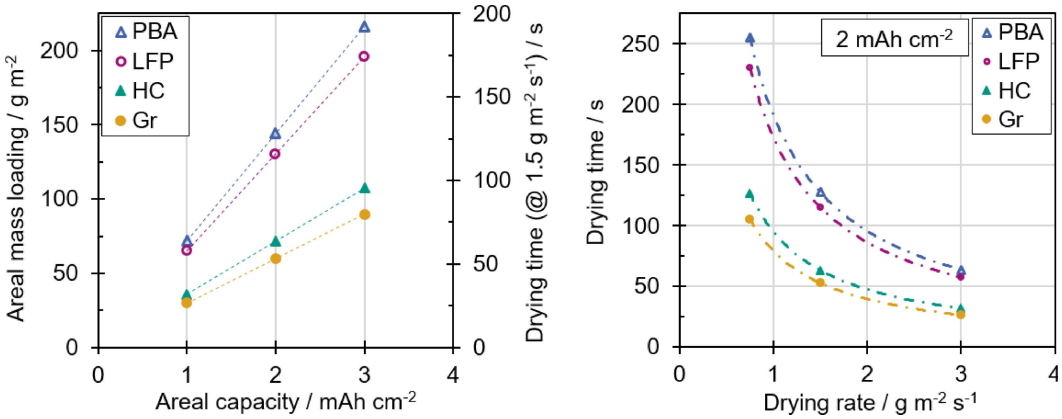

Figure 2. Calculated areal mass loading and drying time as a function of the areal capacity (93 wt-% active material share in the dry electrode, 43 wt-% solid content in the slurry) and a constant drying rate of 1.5 g m^{-2} s^{-1} as considered an industrially relevant drying rate[30,39] (left). For the calculation of the areal mass loading, the capacities in Table 1 were used. Figure 2(right) shows the calculated drying time as a function of the drying rate for 2 mAh cm^{-2}. The drying time difference between LIB and SIB materials is closer for higher drying rates. At a drying rate of 3 g m^{-2} s^{-1}, the drying time for anodes is in the range of 26–32 s (Gr vs. HC) and for cathodes in the range of 58–64 s (LFP vs. PBA).

large differences in production speed arise from an apparently small difference in drying time. Table 2 shows a comparison of the production speed for a given dryer with a length of 50 m and, on the other hand, dryer length for a production speed of 50 m min^{-1}. The comparison in both cases is made for a fixed drying rate of 3 g m^{-2} s^{-1} and an areal capacity of 2 mAh cm^{-2}. For the assumed drying rate of 3 g m^{-2} s^{-1} a production speed of about 50 m min^{-1} is possible for all investigated anodes and cathodes for an areal capacity of 2 mAh cm^{-2}.

As noted, the production speeds and dryer length between LIB and SIB electrode manufacturing can only be similar if the drying of SIB slurries will be higher than for LIB slurries. The needed increase of the drying rate directly corresponds to the decrease in the specific capacity. In this case, LFP has a specific capacity higher than PBA by a factor of 1.2 and Gr higher than HC by a factor of 1.1. The drying rate must be increased by this factor for the same production speed or dryer length for the SIB materials. This means that especially for high throughput and, thus, a high level of drying rate for LIB the drying rate for SIB would be even higher. This correlation can also be applied to compare other active materials against each other (e.g., LFP vs. lithium nickel manganese cobalt oxide). The question arises how higher drying rates affect the SIB electrodes' quality. This will be addressed more in detail in the section about adhesion.

Table 2. Overview of two case studies for electrodes with an areal capacity of 2 mAh cm^{-2} and dried at a constant drying rate of 3 g m^{-2} s^{-1} for Gr vs. HC and LFP vs. PBA: Electrodes' manufacturing speed for a fixed dryer length of 50 m or, on the other hand, expected dryer length for a fixed production speed of 50 m min^{-1}.

	Gr	HC	LFP	PBA
Production speed [m min^{-1}] @ fixed dryer length of 50 m	114	95	52	47
Dryer length [m] @ fixed production speed of 50 m min^{-1}	22	26	48	53

Another way to compensate the differences between LIB and SIB is to adjust the active mass fraction or solid content. The solid content seems like an easily adjustable variable in the process for the same composition, but it has not been clarified how this affects the processing of the individual materials in terms of mixing, viscosity, coating and drying and is not the scope of this study. It is shown in the literature that higher solids content can lead to an increase in adhesion.[56] However, the study of slurry viscosity in the next section shows that increasing the solid content would affect the properties of LIB and SIB slurries differently due to the particles' properties.

Viscosity profiles for water-based LIB and SIB slurries

To compare the different active materials, the slurries for Gr, HC, LFP and PBA were produced with the same solid content of 43 wt-% using the identical manufacturing procedure and mixing parameters. Figure 3 shows the viscosity profiles as a function of the shear rate in a double logarithmic plot.

Figure 3 shows that the viscosity of the SIB anode and cathode slurries is higher compared to the investigated LIB materials at low shear rates (0.1–10 s^{-1}) with identical composition and mixing parameters. To give a more detailed discussion of the viscosity profiles, Table 3 shows the average particle diameter, the density, and the BET surface of the materials. It also shows an overview of the different volume fractions of the active materials in the slurry due to their densities. The calculation of the active materials' volume fraction is given in the Experimental Section using Equation (9).

On the one hand, the viscosity profile can be attributed to the smaller particle size of the anode for SIB. We refer here to the average particle diameter as the comparison parameter between the different materials. Amongst that certainly, the particle size distribution and particle shape also influence the viscosity behavior, especially at low shear rates. Round particles are more likely to slide past each other, whereas irregularly

© 2023 The Authors. Batteries & Supercaps published by Wiley-VCH GmbH

25666223, 2023, 11, Downloaded from https://chemistry-europe.onlinelibrary.wiley.com/doi/10.1002/batt.202300291 by Cochrane Germany, Wiley Online Library on [20/12/2023]. See the Terms and Conditions (https://onlinelibrary.wiley.com/terms-and-conditions) on Wiley Online Library for rules of use; OA articles are governed by the applicable Creative Commons License

Research Article
doi.org/10.1002/batt.202300291
Chemistry Europe
European Chemical Societies Publishing

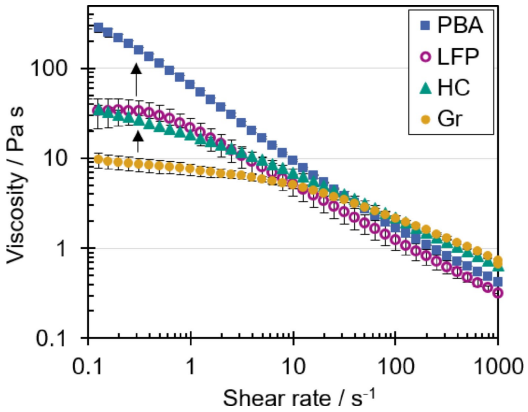

Figure 3. Viscosity profile as a function of the shear rate of LIB and SIB anodes and cathodes measured at 25 °C. The figure shows a comparison of Gr vs. HC anodes and LFP vs. PBA cathodes with identical water-based slurry composition, mixing procedure and solid content. The viscosity of the SIB anode and cathode slurries shows at low shear rate of 0.1 s^{-1} a higher viscosity compared to the LIB slurries.

shaped particles might interact more.[57] Hence, LFP is expected to have a lower viscosity in the low shear range than PBA. On the other hand, the volume fraction of the active material in the slurry depends on the density of the material. With a higher volume fraction of the active material, the flow resistance in the slurry increases and therefore the viscosity at lower shear rate. From the measurement of viscosity as a function of the shear rate, it is not possible to infer directly which factor described leads to the difference between LIB and SIB materials as it is a superposition of several effects, that favors a higher viscosity for the investigated SIB materials.

A higher viscosity in the low shear rate region means that particle interactions are increased. It should be noted that a high viscosity at low shear rates is advantageous, as this limits particle movement (less susceptible to sedimentation). Towards higher shear rates ($>10\ s^{-1}$) the viscosity of the anode and the viscosity of the cathode slurries approach each other indicating a comparable suitability for slot-die coating.[10,33,58] A further effect is that scrap rates due to edge elevations during electrode manufacturing can be minimized by slurries with a higher viscosity at low shear rates and shear thinning behavior.[33,58–60]

As suggested in the previous section, the different drying times may be compensated by increasing the solid content for SIB materials with a lower capacity than LIB materials. However, it can be seen from the determination of viscosity that an increase in solid content, with otherwise the same composition between LIB and SIB, leads to a further increase in viscosity. A too high viscosity at lower shear rates could be challenging for pumping the slurries. It is to be expected that the entire profile of the viscosity curve is shifted to higher values, which also leads to a different viscosity at the shear rate in the coating process. This could lead to a stronger difference in coating and stability behavior between LIB and SIB. This can also affect the design of the slot die cavity and may result in the need for new coating dies.[61] In addition, air bubbles contained in the slurry, which interfere with the subsequent coating process and lead to defects in the coating, could be more difficult to remove due to a higher viscosity. Certainly, the formulation for anode and cathode may need to be adjusted to get the best from the material depending on the application. This also affects the viscosity profile as well as coating and drying effects. The effect of viscosity during microstructure formation will be discussed in the next section.

Microstructure formation

One of the first parameters to be considered in the production of electrodes is the setting of the necessary wet film thickness. Typically, electrodes are produced with a specific areal mass loading or dry mass per unit area. However, for coating with a coating tool such as a slot die, the resulting wet film thickness and the slurry mass per unit area is crucial due to the conservation of mass to receive the desired electrode from the total volume flow, the production speed and the width of the coating. A challenge in increasing the production speed for active materials with lower specific capacity is not only the increased drying rate at constant dryer length and a considerably higher wet coating weight, but also the volume flows of slurry as well, which not only depend on the capacity of the active material, but on density as well. The difference in particle density influences not only the slurry flow behavior but also the needed volume flow and the coating thickness (wet coating and porosity). According to Equation (4) the wet film thickness can be calculated by the desired areal mass loading divided by the solid content of the slurry and the density of the slurry (Table 3).

$$h_{wet} = \frac{m_{area}}{x_{solids}} \cdot \sum \frac{x_j^{slurry}}{\rho_j} \tag{4}$$

Table 3. Overview of the average particle size, density (measured by gas pycnometry), and BET surface of the LIB and SIB materials. The volume fraction of the active material in the slurry with the same composition is also given.

	Particle diameter x_{50} [µm]	BET surface [$m^2\,g^{-1}$]	Density [$kg\,m^{-3}$]	Volume fraction slurry [% ($m^3\,m^{-3}$)]
Gr	18	2.7	2260	22.9
HC	9	3.5	2062	24.6
LFP	13	24.0	3350	16.7
PBA	12	1.0	2049	24.7

© 2023 The Authors. Batteries & Supercaps published by Wiley-VCH GmbH

25666223, 2023, 11, Downloaded from https://chemistry-europe.onlinelibrary.wiley.com/doi/10.1002/batt.202300291 by Cochrane Germany, Wiley Online Library on [20/12/2023]. See the Terms and Conditions (https://onlinelibrary.wiley.com/terms-and-conditions) on Wiley Online Library for rules of use; OA articles are governed by the applicable Creative Commons License

Research Article
doi.org/10.1002/batt.202300291
Chemistry Europe
European Chemical Societies Publishing

Figure 4 shows the wet film thickness of LIB and SIB materials as a function of the areal capacity.

With increasing areal capacity, the difference in electrodes' wet film thickness between LIB and SIB materials increases as expected from Figure 2. For 1–3 mAh cm^{-2} the wet coating thickness is about 23% higher for SIB than for LIB anodes and cathodes. The percentage change is the same for anodes and cathodes and areal capacities, but the absolute differences in wet coating thickness increase for higher areal capacities. In comparison to the areal mass loading from Figure 2, differences between the materials are increased as the wet film thickness is also depending on the volume fraction of the material and, with that, on the density. It is therefore noteworthy that the wet film thicknesses of PBA and LFP differ more than the required areal mass loading would suggest. Depending on existing equipment, higher wet film thicknesses could mean additional investment for larger mixers, feed tanks, etc. Certainly, if a configuration in a production line has been made for high-capacity electrodes, for example, the production of larger volumes or even the pumping of higher volume flows is not a challenge. To give an overview of the possibilities: A reduction of the wet film thickness can be achieved in general by a higher active material content, solid content, specific capacity, or a higher density of the active material.

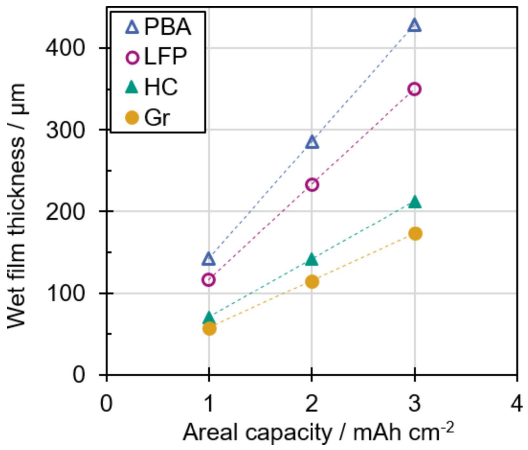

Figure 4. Calculated wet film thickness as a function of the areal capacity. For the calculation of the thicknesses, the areal mass loadings from Figure 1 are used. With increasing areal capacity, the difference in wet film thickness between LIB and SIB materials for the anode and cathode increases. Besides the capacity and the electrodes' composition, the wet film thickness depends on the density of the active material. For 1–3 mAh cm^{-2}, the wet film thickness of SIB anodes is about 23% higher and of SIB cathodes about 22% higher than for LIB.

To investigate the adhesion for the different materials as a function of the areal capacity different areal mass loadings were coated, and the electrodes characterized. The dry film thickness, the areal mass loading and the porosity are given in Table 4.

As expected, the areal mass loading and the dry film thickness of SIB materials are higher than for LIB materials at about the same areal capacity. The resulting porosity shows the influence of the different particle sizes and particle densities. It is known from the literature that the drying rate has no effect on the porosity of the electrode for Gr and HC. This could also be confirmed here for all material systems. The data for ~2 mAh cm^{-2} is averaged from electrodes produced at different drying rates (next section).

In any case, from about 1 mAh cm^{-2}, the porosity is higher than at ~2 or 3 mAh cm^{-2}. Lower porosity with increasing areal capacity has been shown for Gr anodes in the literature and it is hypothesized therein that a denser particle network forms with increasing electrode coating thickness, because more time is available for an ideal arrangement of the particles (at the same drying rate).[62] This would imply that porosity is also affected at different drying rates. However, this is not the case in this study and others, so we assume that this cannot be an appropriate explanation. Another possibility are edge effects as the particle arrangement at the current collector is not the same as inside the porous electrode as it is restricted by the plane surface of the current collector. Given a stacking of only several particles over each other for all materials investigated this may play a major role here especially for the very thin electrodes with 1 mAh g^{-1}. It is noted that the average porosity for electrodes made of Gr, HC and LFP for areal capacities between 2–3 mAh cm^{-2} have a similar porosity of about 58% for the same formulation. However, this does not necessarily mean that the drying behavior is the same.

This is pointed out when the solvent loading at the end of film shrinkage is calculated. This solvent loading and the starting of the pore emptying process play an important role especially if a multi-stage drying profile is to be run. With the film porosity as well as the density of the solvent and the density of the dry mixture of the materials used, the solvent

Table 4. Overview of dry coating thickness, areal mass loading and electrode porosity for a target areal capacity of 1, 2 and 3 mAh cm^{-2} for Gr vs. HC and LFP vs. PBA. The data for 2 mAh cm^{-2} are average values for different drying rates. As known from the literature, the porosity of electrodes, for example, does not change during drying at different drying rates.

	Gr			HC			LFP			PBA		
Areal capacity [mAh cm^{-2}]	1	2	3	1	2	3	1	2	3	1	2	3
Dry coating thickness [µm]	36±3	67±3	101±3	56±5	93±1	143±4	70±4	104±2	152±5	72±6	128±2	162±7
Areal mass loading [g m^{-2}]	29±1	60±1	91±1	40±2	76±1	118±2	79±9	130±2	200±2	77±1	155±3	210±4
Density dry mixture [kg m^{-3}]	2136			1970			2992			1959		
Electrode porosity [%]	62±1	58±2	57±1	64±1	58±1	58±1	62±2	58±1	56±1	47±1	38±1	33±2
Solvent loading X_{EOFS} [g g^{-1}]	0.77	0.64	0.63	0.88	0.70	0.70	0.55	0.46	0.43	0.44	0.31	0.25

© 2023 The Authors. Batteries & Supercaps published by Wiley-VCH GmbH

25666223, 2023, 11, Downloaded from https://chemistry-europe.onlinelibrary.wiley.com/doi/10.1002/batt.202300291 by Cochrane Germany, Wiley Online Library on [20/12/2023]. See the Terms and Conditions (https://onlinelibrary.wiley.com/terms-and-conditions) on Wiley Online Library for rules of use; OA articles are governed by the applicable Creative Commons License

Research Article
doi.org/10.1002/batt.202300291
Chemistry Europe
European Chemical Societies Publishing

loading at the end of film shrinkage can be calculated by [Equation (5)].

$$X_{\text{End of film schrinkage}} = \frac{\varepsilon}{1-\varepsilon}\frac{\rho_{\text{solvent}}}{\rho_{\text{dry mixture}}} \quad (5)$$

If we assume that the onset of binder migration coincides with the onset of pore emptying, which in turn coincides with the end of film shrinkage, then the onset of binder migration is both dependent on porosity and on the density of the dry mixture, which changes for different active materials for electrodes with the same composition. To illustrate the relationship of the solvent fraction at the end of film shrinkage for all material systems, Figure 5 shows the normalized decrease in film thickness during drying amongst the concentration of CMC solution (relative to solvent fraction in the slurry). A porosity of 58% for Gr, HC, LFP and 40% for PBA is assumed for this purpose. The calculation is based on the change of the volume fractions due to the evaporation of the solvent during drying. As the same formulation and solid content were used for all material systems, the solid content used corresponds to a loading of $X_{t=0} = 1.33\ g_{solvent}\, g_{dry\,electrode}^{-1}$ for all materials.

The film thickness decrease shows the decrease of the wet film thickness until the end of film shrinkage, that is when the capillary network is fully saturated with CMC solution. It can be seen, as stated, that the solvent fraction at the end of film shrinkage and, thus, the concentration of the CMC related to the solvent fraction in the slurry is different for all material systems. Two regimes appear, one for the anodes and one for the cathodes. The difference for Gr and HC results only from the density of the materials as the porosity of 58% is the same. As the porosity determinations show experimental variations the calculation should be used with caution. In general, however, it can be concluded for each material system that with decreasing porosity the solvent content at the end of film shrinkage is also lower and the concentration of the CMC solution is higher. For areal capacities of 2–3 mAh cm^{-2}, the solvent loading for the end of film shrinkage for Gr and HC ranges from 0.63 to 0.70. For LFP, this value of about 0.45 is considerably lower due to the higher density of the dry mixture. The differences clearly show that for a multistage drying profile, the first critical time for transition from a high to a low drying rate for cathodes can happen at lower solvent fractions, which is necessary to design the drying process to achieve higher drying rates. Assuming this point in time coincides with the end of film shrinkage, which is not necessarily the case. For a more agile production line, this means that more measurement equipment is needed in the dryer (film thickness measurement, for example) to be able to adjust the drying profile to new materials.[63] The process must be able to adapt to the conditions of the materials. Here, one advantage of a longer dryer may be to have more control and flexibility where to change the drying rate exactly in the drying process.

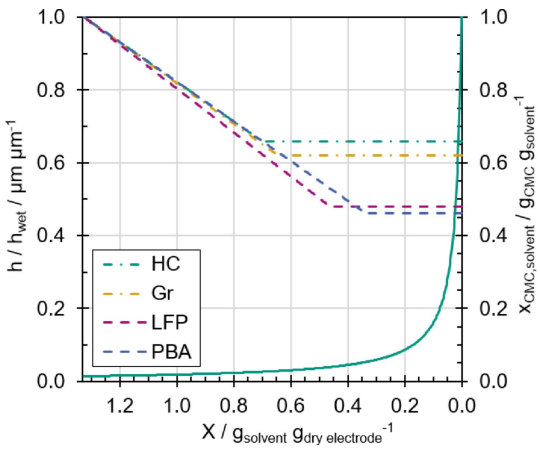

Figure 5. Calculated film thickness as a function of the solvent loading from wet film thickness to the end of film shrinkage. The calculation is based on the change in volume fraction due to the evaporation of the solvent during drying. It shows only the part from the beginning of the drying process to the end of film shrinkage. Additionally, the mass fraction of CMC/solvent as a function of the solvent loading is given. The solvent loading for all material systems is different at the end of film shrinkage and so are the CMC concentrations.

Hence the different solvent loading at the time of the latest onset of pore emptying, the concentration of CMC related to the solvent can differ significantly too. For HC and Gr, the concentration is approximately 2.4–2.7 wt-%, and for LFP and PBA 3.9–5.2 wt-%, respectively. Since the relationship between the concentration and the viscosity of the CMC solution is exponential, a lower solvent loading inevitably leads to a higher viscosity at the time of the end of film shrinkage. It is to be investigated whether this may affect the capillary pore emptying mechanism or not. Furthermore, CMC can undergo a phase separation to form a polymer-rich phase and a polymer-poor or solvent-rich phase depending on the temperature and concentration.[64] This could result in solvent movement independent of CMC and SBR during drying prior to the end of film shrinkage or during capillary transport. Consideration of the conditions of CMC during drying of different material systems and for different drying rates could provide deeper insight into the drying behavior and properties of the electrodes. However, a more in-depth consideration of this effect is not the subject of this study as it focuses on material effects on the process in general. It is evident, that the differences in drying behavior have an impact on the development of electrode properties like adhesion with increasing drying rate.

Adhesion depending on areal capacity and drying rate

From the previous sections, the question arises how the electrode properties and the binder migration are affected by the differences in microstructure formation of different particle systems and areal capacities (different porosity, layer thickness). As shown, for similar production speed, SIB materials with lower capacities must be dried at higher drying rates depending on the areal capacity. It is therefore important to determine how the electrodes behave when slurries of all materials are dried at increasing areal capacity and increasing drying rate at fixed areal capacity. As an indirect measure for binder migration, the adhesion force of the electrodes is measured, respectively.

© 2023 The Authors. Batteries & Supercaps published by Wiley-VCH GmbH

25666223, 2023, 11, Downloaded from https://chemistry-europe.onlinelibrary.wiley.com/doi/10.1002/batt.202300291 by Cochrane Germany, Wiley Online Library on [20/12/2023]. See the Terms and Conditions (https://onlinelibrary.wiley.com/terms-and-conditions) on Wiley Online Library for rules of use; OA articles are governed by the applicable Creative Commons License

Research Article
doi.org/10.1002/batt.202300291
Chemistry Europe
European Chemical Societies Publishing

Figure 6(left) shows the adhesion force for increasing areal capacity (fixed drying rate), and Figure 6(right) shows the adhesion force as a function of the drying rate to investigate binder migration (fixed areal capacity). Figure 6(left) shows a significant difference in the adhesion force for the material systems used. All materials show a decrease in adhesion force compared to the lowest areal capacity. On the one hand the adhesion force decreases approximately linearly for Gr and PBA and, on the other hand, LFP and HC show no further deterioration from 2–3 mAh cm^{-2}. Noticeable are the different levels of absolute adhesion force for the active materials. However, permissible for direct comparison are only the absolute adhesion forces of HC, LFP and PBA as Gr is coated on a copper substrate instead of aluminum.

Comparing LFP and HC, LFP shows a higher adhesion force over the complete range of areal capacities. As described in the previous section, the concentration of CMC at the end of film shrinkage, as the possible starting point of binder migration, is higher for LFP electrodes. This means that there could be a higher resistance for the capillary transport and, thus a resistance for advective transport of SBR, which mainly provides adhesion. However, PBA shows a higher CMC concentration compared to LFP at the end of film shrinkage, but a much lower adhesion force. It must be noted that PBA electrodes with the specified composition show first cracking at the highest areal mass loading set, which means that the cohesion is of concern. The PBA electrodes feel brittle after drying and have a tendency for delamination from the current collector due to cracks developing in the coating especially for the highest areal capacity. The adhesion force may not be fully comparable with the other systems. However, to explain the different behavior there must be another super-positioning effect that decreases the adhesion of PBA down to the measured level. This hypothesis is further backed up by the comparison of the porosity and the adhesion forces for increasing areal capacity. A higher adhesion force for the lowest areal capacity in all cases contradicts with an explanation by a less pronounced capillary transport due to reaching the end of film shrinkage at lower solvent loading. As similar explanation in the literature, it is presented, that for thicker electrodes the onset of pore emptying occurs before the end of film shrinkage and is thus more disruptive.[62] If this was the case then a plateau in adhesion force would not be expected for both LFP and HC. One fitting explanation for all three cases can be found in the materials properties. It suggests that for HC, LFP and PBA the adhesion force follows the trend of the BET surface that is the smallest for PBA. This can be misleading, since it has also been shown that adhesion can be lower with a higher BET surface.[11,12,14] The BET surface can be increased by accessible pores inside the particles (particle porosity), which is for example the case for LFP used. The differences in adhesion could be related to the interaction of the specific surfaces' functional part only, that can interact with binders causing fixation of CMC/SBR. This interaction of the materials and with the substrate need to be further investigated to better describe the dependence of the adhesion force for different material systems.

The hypothesis that SBR is less mobile due to the stronger binding of CMC to smaller particles[10,13] or the functional part of the specific surface will be further discussed when discussing the adhesion force of the different systems with increasing drying rate: One could hypothesize that for increasing drying rate, i.e., by applying more driving force for capillary transport, LFP and HC electrodes could provide better fixation of the CMC as resistance against advective SBR transport and, thus, less decrease in adhesion force. Figure 6(right) shows the adhesion force with increasing drying rate for all material systems. The first value (100%) at a drying rate of 0.75 g m^{-2} s^{-1} corresponds to the value of the adhesion force from Figure 6(left) at 2 mAh cm^{-2}.

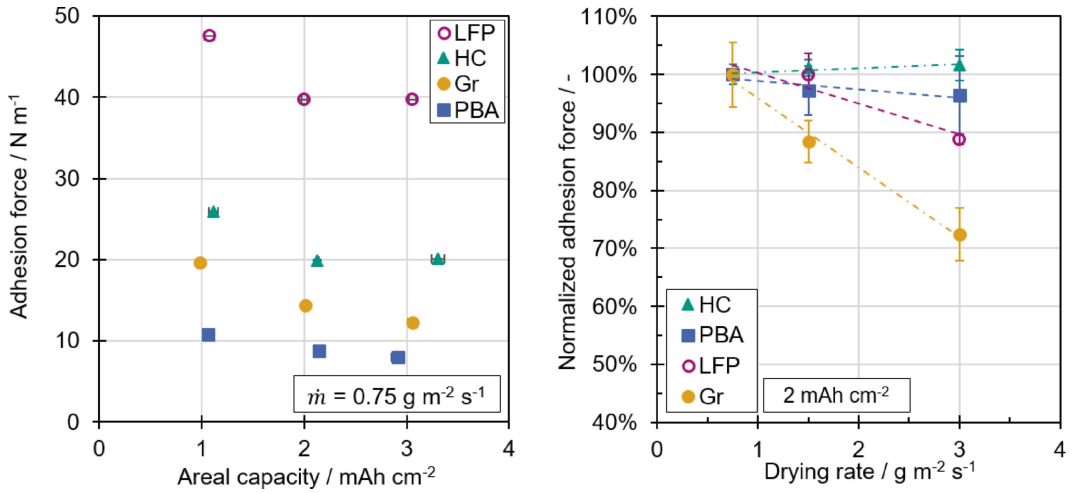

Figure 6. Adhesion (90° peel test) as a function of the areal capacity for LIB and SIB anodes and cathodes at a low drying rate of 0.75 g m^{-2} s^{-1} (left). Adhesion as a function of the drying rate for an areal capacity of 2 mAh cm^{-2} (right). LFP, PBA and HC are coated on aluminum and Gr on copper substrate. The electrodes of the different material systems show different adhesion forces at all areal capacities investigated, although all electrodes have the same binder content. A higher areal capacity results in a lower adhesion force for all electrodes. Surprisingly, some electrodes show less binder migration than others (right). Especially in the case of HC there is no negative influence of the drying rate on the adhesion force. The PBA electrodes also indicate a lower effect of drying rate on adhesion force, but cracking also occurred at higher drying rates.

© 2023 The Authors. Batteries & Supercaps published by Wiley-VCH GmbH

25666223, 2023, 11, Downloaded from https://chemistry-europe.onlinelibrary.wiley.com/doi/10.1002/batt.202300291 by Cochrane Germany, Wiley Online Library on [20/12/2023]. See the Terms and Conditions (https://onlinelibrary.wiley.com/terms-and-conditions) on Wiley Online Library for rules of use; OA articles are governed by the applicable Creative Commons License

Research Article
doi.org/10.1002/batt.202300291
Chemistry Europe
European Chemical Societies Publishing

Especially the Gr electrodes show a decrease in adhesion force by about 30% with an increasing drying rate. Due to the faster drying, the capillary transport also proceeds faster and, thus, the volume flow of the solvent in the pores increases. It would be conceivable that, depending on the drying rate, the proportions of binder that are weakly bond on the particles or substrate change and remains in the same position until the end of drying and a mobile binder fraction, which can be transported if the capillary transport is disruptive enough.[12] Another possibility is that, depending on the drying conditions and the particle system, the start for capillary transport is reached at a different time.[65] It is also discussed in the literature that a concentration gradient can built up in the liquid phase from the beginning of the drying until the time when the end of film shrinkage is reached. This gradient could be less pronounced during slower drying making the capillary emptying less pointed into the direction of the gradient towards the current collector.

HC in comparison to Gr does not show any negative influence but little positive effect of the drying rate on the adhesion force. The LFP electrodes show a similar behavior. Up to a drying rate of 1.5 $g\,m^{-2}s^{-1}$ faster drying has no negative influence on the adhesion force. For 3 $g\,m^{-2}s^{-1}$ the adhesion force decreases by 10%. This is surprising, since the observation before had shown that the electrodes behave similarly to HC with increasing areal mass loading and in general have a higher adhesion force. The behavior of HC and LFP supports the hypothesis from the investigation of different areal capacities, that the CMC concentration cannot be the explanation for the development of the adhesion force, as the earlier entrance into the capillary transport should lead to more SBR binder migration for HC. Nevertheless, the higher drying rate does not appear to result in a lower adhesion force or cracking for HC electrodes. This suggests that the interaction between the binders and the particles has a strong influence on the movement of CMC and SBR. In the case of LFP and HC, the smaller particle size of HC seems to be the more pronounced effect for the fixation of binder at increasing drying rate compared to the BET-surface. In conclusion, this means that in the case of HC, a better fixation of the binder can lead to a lower absolute adhesion force, but vice versa less SBR is transported even with increased capillary transport due to higher drying rates. One explanation is that the particle size of LFP is higher than for HC and, thus, the fixation of the binder system to the particles and the substrate may be less developed and the free SBR proportion is larger. Due to the increase in the driving force for capillary transport (higher drying rate), the binder in the LFP electrode can be transported above a certain threshold value for the drying rate and, thus, reduces the adhesive force. For the LFP electrodes, an interesting aspect would be to investigate the adhesion at increasing drying rates by adding smaller LFP particles. The assumption would be that this could also reduce binder migration at higher drying rates.

Bending stiffness: Two-point bending test

As described, the LFP and PBA electrodes show a higher stiffness than HC and Gr due to their higher film thickness. Especially, PBA electrodes tend to delaminate, and the electrodes feel brittle, noticeable of the physical handling of the electrodes. As a quantitative measure, this stiffness can be evaluated by measuring with a two-point bending test to compare materials at different areal loadings. It is not the objective to specify a stiffness value at which an electrode can no longer be processed. This is highly dependent on the machines and production parameters used. However, the measurement allows a quantitative comparison and could be linked to possible future roll-to-roll electrode processing. In order to compare the electrodes' behavior for different materials and areal capacity, the bending stiffness is shown in Figure 7.

The higher the areal capacity (high mass loading and high thickness), the higher the bending stiffness. For all areal capacities, the Gr anode has the lowest bending stiffness. The Gr anode was coated on a 10 μm copper foil, while the other electrodes were coated on a 20 μm aluminum foil (the bending stiffness of the copper foil is lower by a factor of 3.25 than the aluminum foil). Furthermore, the Gr anode has the lowest dry film thickness, which could be a reason for the low bending stiffness. For all areal capacities the PBA cathode has the highest bending stiffness and the highest dry film thickness. At 3 $mAh\,cm^{-2}$, the PBA cathode has a bending stiffness nearly 2 times higher than the LFP cathode. For the areal capacities of 1 and 2 $mAh\,cm^{-2}$ the values for the HC anode and the LFP cathode are almost the same. When increasing the areal mass loading is increased to 3 $mAh\,cm^{-2}$ the bending stiffness of LFP is about 10.4 times higher than that of HC. The dry film thicknesses of LFP are also higher than for HC. The correlation between bending stiffness and areal mass loading of Gr and HC

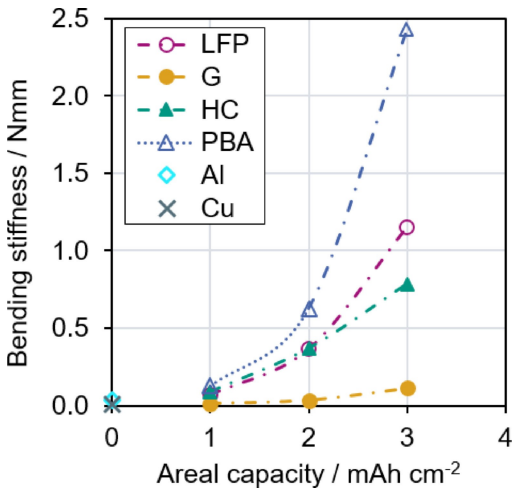

Figure 7. Bending stiffness as a function of the area capacity. LFP and PBA with the highest film thickness show higher values for the bending stiffness. With increasing areal capacity and film thickness, the bending stiffness increases for all material systems. Aluminium has a higher bending stiffness than copper for the substrates investigated.

© 2023 The Authors. Batteries & Supercaps published by Wiley-VCH GmbH

25666223, 2023, 11, Downloaded from https://chemistry-europe.onlinelibrary.wiley.com/doi/10.1002/batt.202300291 by Cochrane Germany, Wiley Online Library on [20/12/2023]. See the Terms and Conditions (https://onlinelibrary.wiley.com/terms-and-conditions) on Wiley Online Library for rules of use; OA articles are governed by the applicable Creative Commons License

25666223, 2023, 11, Downloaded from https://chemistry-europe.onlinelibrary.wiley.com/doi/10.1002/batt.202300291 by Cochrane Germany, Wiley Online Library on [20/12/2023]. See the Terms and Conditions (https://onlinelibrary.wiley.com/terms-and-conditions) on Wiley Online Library for rules of use; OA articles are governed by the applicable Creative Commons License

can be interpreted as linear in the range investigated. For higher areal capacities than investigated it is expected that the behavior is exponential as for LFP and PBA. Over all, the bending stiffness appears to be dependent on the dry film thickness as it increases steadily with the dry film thickness for all materials tested.

A comparison with the adhesion force reveals two findings: first, the general finding that a decrease in adhesive force leads to an increasing bending stiffness; second, the tendency that an overall high adhesive force (LFP > HC > Gr) also leads to an overall high bending stiffness. However, for the PBA the adhesive force was lower than for Gr, but the bending stiffness was the highest for all materials.

Günther et al.[53] and also our own experience have shown that stiff electrodes are difficult to guide around deflection rollers and are more likely to show web tears. During calendering the stiffness of the electrodes increases again and the risk of web tears is increased.[53] For an industrial coating it may be necessary to improve the composition of the PBA electrodes to provide a higher adhesion force and less brittle behaviour. As with the adhesion measurement, however, it should be noted that the results of the bending tests for PBA may not be completely reliable as the samples for higher areal loading were already covered with cracks and small delamination at on the edge before the testing.

Conclusions

The active materials of LIB and SIB anodes and cathodes differ in particle morphology as well as in capacity. Due to the difference in specific capacities for the anode and cathode materials, the areal mass loading, coating- and electrode thicknesses and, especially, the drying times are different for LIB and SIB electrodes at the same areal capacities. This can have a great impact on the process chain. An important point to note is that if the composition of the slurry is the same, the drying times will differ by the factor of the specific capacities. Depending on the electrode manufacturing speed, even small differences in drying time can lead to significantly different dryer length for LIB and SIB anodes and cathodes, especially at higher drying rates. In other words, for a given coating and drying equipment, lower production speeds can be run for the SIB materials investigated in this study if the process parameters of the dryer are not changed. In any case, it would be possible to produce SIB electrodes at the same production speed or even faster than LIB electrodes on a given coating and drying machine, if the drying rate can be increased. Therefore, one goal for the future, especially for SIB, should be the production of electrodes with higher drying rates.

Comparing the adhesion force evolution with increasing drying rates for 2 mAh cm^{-2} LIB and SIB electrodes, especially HC but also LFP electrodes can be produced at higher drying rates without adhesion changes. Together with the investigations in the literature, it is considered that the LFP and HC electrodes show less binder migration due to the interaction of the active material with the binder system, and the microstructure formation during the pore emptying process. The interaction of the binder system with the active materials and the substrate need to be further investigated in the future to gain a better understanding and evidence for the hypotheses that have been made. In the case of PBA, the results show that the processing at industrially relevant drying rates is possible, but the overall adhesion and cohesion are reduced and need to be optimized by formulation studies to overcome the brittle behavior and issues with crack formation.

The bending stiffness increases with increasing areal capacity and therefore dry film thickness. Adhesion and porosity may influence the bending stiffness, but the correlations still seem to be complex. More tests are needed to make fully reliable statements on the correlations.

For the particle design, the drying behavior of electrodes should also be included in the future. This could result in a lower decrease in adhesion with increasing areal mass loading and less binder migration at increasing drying rate. When using smaller particles or a higher proportion of small particles, the binder migration can probably be mitigated. In addition to studies on Gr and HC in the literature, this needs to be demonstrated for other systems such as LFP and other active materials. As an alternative approach, multilayer architectures (electrode design) with different particle morphologies have to be investigated to achieve the desired electrode properties combined with fast fabrication.

Experimental Section

Material characterization

The specific surface areas were obtained by BET measurements using nitrogen adsorption gas (Gemini VII 2390, Micromeritics). The density of the materials was measured by helium pycnometry (AccuPyc 1330, Porotec). The particle size was determined by laser diffraction (Horiba LA950, Retsch Technology). For this purpose, the active materials are dispersed in 2-propanol. A Zeiss Supra 55 from Carl Zeiss AG (Oberkochen, Germany) was used for SEM investigations.

Slurry mixing and viscosity

Mixing: The water-based slurries for HC (Kuranode, kuraray), Gr (SMGA, Hitachi Chemical Co. Ltd., Japan), PBA (Gelon LIB Co., Ltd.), LFP (ibu-Tec, Germany) were mixed in a dissolver (Dispermat SN-10, VMA Getzmann GmbH Verfahrenstechnik, Germany). The composition was chosen so that the dry electrode has the composition in Table 5.

Carbon black (Super C65, Imerys) and a 2 wt-% CMC (Sunrose MAC500LC, Nippon Paper Industries, Japan) solution were added to the container and dispersed at 1000 rpm for 30 min. The container was cooled during the entire mixing process. The active material

Table 5. Composition of dry LIB (Gr, LFP) and SIB (HC, PBA) electrodes.

Active material [wt-%]	C65 [wt-%]	CMC [wt-%]	SBR [wt-%]	Solids [wt-%]
93.00	1.40	1.87	3.73	43.00

© 2023 The Authors. Batteries & Supercaps published by Wiley-VCH GmbH

Research Article
doi.org/10.1002/batt.202300291
Chemistry Europe
European Chemical Societies Publishing

particles were added in three equal steps and further dispersed. Additional water was added to reach the final solid content. The slurries were then mixed for 30 min at 1500 rpm. In the final step, SBR (Zeon Europe GmbH, Japan) was added and the slurry was mixed for 10 min at 500 rpm. The container was degassed during the final mixing step.

Viscosity: The viscosity was measured by a rotation viscometer Physica MCR 101 (Anton Paar, Germany) with a plate-plate geometry (25 mm diameter) from 0.01–1.000 s^{-1} at 25 °C.

Electrode coating and drying

The coating and drying of the anode and cathode slurries were carried out in a discontinuous process as described by Baunach et al.[40] The 10 µm copper current collector (Civen Metal Material Co. Ltd., China) for the graphite electrodes or the 20 µm aluminum current collector (Schlenk, Germany) was attached to a temperature-controlled plate via vacuum. The coating of the anode and cathode slurries was applied with a doctor blade ZUA 2000.100 (Zehntner) and subsequently the coating was run under the drying nozzles of an impingement dryer. For homogeneous drying, the plate was periodically moved under the dryer. For all experiments, the drying rate was determined by the temperature of the heated plate and the heat transfer coefficient of the slot nozzle dryer, considering the dew point of the drying air. The solvent removal of a thin wet film is in general governed by heat and mass transfer in the gas phase, the phase equilibrium and the diffusion in the wet film. In the case of electrode drying, the mass transfer in the gas-phase is the rate determining step. Consequently, the consideration of gas-phase mass transfer is sufficient to describe the electrodes' drying process. The mass transfer in the gas-phase can be described according to Equation (6), assuming unilateral diffusion in a binary system.

$$\dot{m}_s = \beta_{s,g}\,\tilde{\rho}_g\,\tilde{M}_s \ln\left(\frac{1-\tilde{y}_{s,dryer}}{1-\tilde{y}_{s,surface}}\right) \tag{6}$$

The drying rate depends on the molar mass of the solvent $\tilde{M}_s$, the molar density of the gas phase $\tilde{\rho}_g$, the mass transfer coefficient $\beta_{s,g}$, as well as the molar fractions of the solvent in the surrounding gas phase $\tilde{y}_{s,dryer}$ and at the phase boundary of the electrode $\tilde{y}_{s,surface}$. It is important to emphasize that the drying rate is closely dependent of the air flow, the gas and film temperature and the solvent loading of the gas phase. Drying temperature affects $\beta_{s,g}$, $\tilde{y}_{s,surface}$ and $\tilde{\rho}_g$ while the air flow changes $\beta_{s,g}$ only. For the batch-drying set up used in this study, the drying rate is set by the film temperature to ensure comparable data to a roll-to-roll process. Table 6 shows the drying rates and the drying or film temperatures for the experiments in this study. Further information on the drying temperature and the drying rate are given in the literature.[10–12,66]

Table 6. Overview of the drying rate and the drying temperature with a constant heat transfer coefficient of 35 $W m^{-2} K^{-1}$. The temperature of the drying slurry corresponds to the film temperature. The average dew point for the experiments was 5 ± 2 °C.

Drying rate [$m^{-2} s^{-1}$]	Drying and film temperature [°C]
0.75	31
1.5	40
3	51

Electrode characterization

The porosity [Equation (7)] was calculated from the areal mass loading divided by the dry coating thickness and the density of the dry mixture of the components [Equation (8)].

$$\varepsilon = 1 - \frac{m_{electrode}}{\rho_{dry\ mixture}\ h_{dry}} \tag{7}$$

$$\rho_{dry\ mixture} = \left(\sum \frac{x_i}{\rho_i}\right)^{-1} \tag{8}$$

The components i are all solid materials in the electrodes. The volume fraction of the active material is calculated with Equation (9).

$$\varphi_{active\ material} = \frac{\frac{x_{active}}{\rho_{active}}}{\sum \frac{x_j}{\rho_j}} \tag{9}$$

The components *j* are all solids and the solvent.

Adhesion

To determine the adhesion force between the current collector and the dried electrodes, a 90° peel test was carried out with a universal testing machine AMETEK LS1 (Lloyd Instruments Ltd., UK) and a 10 N load cell. All samples of the dried electrodes were cut out with a width of 30 mm and attached with the coated side to an adhesive strip. The sample was pressed on with a weight of 10 kg to ensure uniform contact between the coating and the adhesive strip. The current collector foil was then peeled off the coating at a constant speed of 600 mm min^{-1} at a 90 ° angle using the testing machine. The resulting pull-off force was measured and divided by the sample width to obtain a line adhesion force.

Two-point bending test

The bending stiffness of the samples was determined by performing two-point bending tests. The measuring equipment (ZwickRoell GmbH & Co. KG) consists of a zwickiLine table-top testing machine and a two-point bending test module for paper and cardboard based on (ISO 5628). The test setup is shown schematically in Figure 8. Four to six measurements can be placed on a single electrode sample strip. As the electrodes are coated on one side, one strip of each material was tested with the coating and one with the substrate inside, as shown in Figure 8(b and c). To compare the materials, the average values of the measurements with the two clamping options were calculated. Additionally, blank substrate

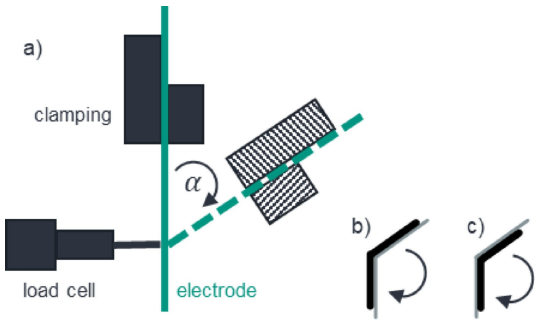

Figure 8. a) Setup of the two-point bending test equipment and clamping options. b) substrate inside, c) coating inside.

© 2023 The Authors. Batteries & Supercaps published by Wiley-VCH GmbH

25666223, 2023, 11, Downloaded from https://chemistry-europe.onlinelibrary.wiley.com/doi/10.1002/batt.202300291 by Cochrane Germany, Wiley Online Library on [20/12/2023]. See the Terms and Conditions (https://onlinelibrary.wiley.com/terms-and-conditions) on Wiley Online Library for rules of use; OA articles are governed by the applicable Creative Commons License

samples were tested. As these are uncoated, only one sample strip was required.

The crosshead moves downwards at a speed of $v = 0.17\ \mathrm{m\,min^{-1}}$. The translational movement is converted into a rotation of the clamping module of the bending angle $\alpha = 0°...90°$. The rotation bends the electrode while it is in contact with the force transducer that transmits the force to the 10 N load cell. The measuring length l is the distance between the clamping and the force transducer. In this setup, the measuring length is $l = 5\ mm$. The result of an experiment is a correlation between force and deflection.

The width-related bending stiffness S is calculated as Equation (10)

$$S = \frac{F}{f} \cdot \frac{l^3}{3b} \tag{10}$$

with the linear deflection f, the referring force F and the sample width b (ISO 5628). In the testXpert III software the quotient $F\,f^{-1}$ is defined as the slope of the Youngs modulus straight line E'. The quotient $F\,f^{-1}$ is therefore calculated in the area of the straight force-deflection curve with the upper and lower force values F_H and F_L corresponding to the limits of the evaluation interval between the upper and lower deflection values f_H and f_L (Equation 11).

$$\frac{F}{f} = E' = \frac{F_H - F_L}{f_H - f_L} \tag{11}$$

The thicknesses of the electrodes were measured using the MarCator 1075R tactile measurement device (Mahr GmbH).

Acknowledgements

This work was funded by the Deutsche Forschungsgemeinschaft (DFG, German Research Foundation) under Germany's Excellence Strategy – EXC 2154 – Project number 390874152 (POLiS Cluster of Excellence). Furthermore, parts of this work were done at the KIT Battery Technology Center (KIT-BATEC) and contributed to the research performed at CELEST (Center for Electrochemical Energy Storage Ulm Karlsruhe). Open Access funding enabled and organized by Projekt DEAL.

Conflict of Interests

The authors declare no conflict of interest.

Data Availability Statement

The data that support the findings of this study are available from the corresponding author upon reasonable request.

Keywords: SIB · post-lithium · LFP · PBA · hard carbon

[1] M.-M. Titirici, P. Adelhelm, Y.-S. Hu, *Sodium-ion batteries. Materials, characterization, and technology: volume 1 et 2*, Wiley-VCH, Weinheim, **2023**.
[2] D. Alvira, D. Antorán, J. J. Manyà, *Chem. Eng. J.* **2022**, *447*, 137468.
[3] J. Peters, A. Peña Cruz, M. Weil, *Batteries* **2019**, *5*, 10.
[4] K. Chayambuka, G. Mulder, D. L. Danilov, P. H. L. Notten, *Adv. Energy Mater.* **2020**, *10*, 2001310.
[5] P. K. Nayak, L. Yang, W. Brehm, P. Adelhelm, *Angew. Chem. Int. Ed.* **2018**, *57*, 102–120.
[6] I. Hasa, S. Mariyappan, D. Saurel, P. Adelhelm, A. Y. Koposov, C. Masquelier, L. Croguennec, M. Casas-Cabanas, *J. Power Sources* **2021**, *482*, 228872.
[7] K. M. Abraham, *ACS Energy Lett.* **2020**, *5*, 3544–3547.
[8] A. Rudola, A. J. R. Rennie, R. Heap, S. S. Meysami, A. Lowbridge, F. Mazzali, R. Sayers, C. J. Wright, J. Barker, *J. Mater. Chem. A* **2021**, *9*, 8279–8302.
[9] M. Reid, "Sodium-ion batteries: disrupt and conquer?", can be found under http://www.woodmac.com/news/opinion/sodium-ion-batteries-disrupt/, **2023**.
[10] J. Klemens, L. Schneider, D. Burger, N. Zimmerer, M. Müller, W. Bauer, H. Ehrenberg, P. Scharfer, W. Schabel, *Energy Techn.* **2023**, 202300338.
[11] J. Klemens, D. Burger, L. Schneider, S. Spiegel, M. Müller, N. Bohn, W. Bauer, H. Ehrenberg, P. Scharfer, W. Schabel, *Energy Techn.* **2023**, 202300267.
[12] J. Klemens, L. Schneider, E. C. Herbst, N. Bohn, M. Müller, W. Bauer, P. Scharfer, W. Schabel, *Energy Technol.* **2022**, 2100985.
[13] J. Kumberg, W. Bauer, J. Schmatz, R. Diehm, M. Tönsmann, M. Müller, K. Ly, P. Scharfer, W. Schabel, *Energy Techn.* **2021**, 202100367.
[14] M. Müller, L. Schneider, N. Bohn, J. R. Binder, W. Bauer, *ACS Appl. Energ. Mater.* **2021**, *4*, 1993–2003.
[15] J. Park, Z.-L. Xu, K. Kang, *Front. Chem.* **2020**, *8*, 432.
[16] L.-F. Zhao, Z. Hu, W.-H. Lai, Y. Tao, J. Peng, Z.-C. Miao, Y.-X. Wang, S.-L. Chou, H.-K. Liu, S.-X. Dou, *Adv. Energy Mater.* **2021**, *11*, 2002704.
[17] I. Hasa, S. Mariyappan, D. Saurel, P. Adelhelm, A. Y. Koposov, C. Masquelier, L. Croguennec, M. Casas-Cabanas, *J. Power Sources* **2021**, *482*, 228872.
[18] M. Thompson, Q. Xia, Z. Hu, X. S. Zhao, *Mater Adv* **2021**, *2*, 5881–5905.
[19] H.-Y. Hu, Y. Xiao, W. Ling, Y.-B. Wu, P. Wang, S.-J. Tan, Y.-S. Xu, Y.-J. Guo, W.-P. Chen, R.-R. Tang et al., *Energy Technol.* **2021**, *9*, 2000730.
[20] T. K. Kumaresan, S. A. Masilamani, K. Raman, S. Z. Karazhanov, R. Subashchandrabose, *Electrochim. Acta* **2021**, *368*, 137574.
[21] H. Au, H. Alptekin, A. C. S. Jensen, E. Olsson, C. A. O'Keefe, T. Smith, M. Crespo-Ribadeneyra, T. F. Headen, C. P. Grey, Q. Cai et al., *Energy Environ. Sci.* **2020**, *13*, 3469–3479.
[22] N. Tapia-Ruiz, A. R. Armstrong, H. Alptekin, M. A. Amores, H. Au, J. Barker, R. Boston, W. R. Brant, J. M. Brittain, Y. Chen et al., *J. Phys. Energy* **2021**, *3*, 31503.
[23] M. Baumann, M. Häringer, M. Schmidt, L. Schneider, J. F. Peters, W. Bauer, J. R. Binder, M. Weil, *Adv. Energy Mater.* **2022**, *12*, 2202636.
[24] P. Gupta, S. Pushpakanth, M. A. Haider, S. Basu, *ACS Omega* **2022**, *7*, 5605–5614.
[25] H. Wu, Y. Chen, T. Wen, L. Chen, X. Pu, Z. Chen, *Batteries* **2023**, *9*, 56.
[26] T. Akçay, M. Häringer, K. Pfeifer, J. Anhalt, J. R. Binder, S. Dsoke, D. Kramer, R. Mönig, *ACS Appl. Energ. Mater.* **2021**, *4*, 12688–12695.
[27] P. Stüble, C. Müller, J. Klemens, P. Scharfer, W. Schabel, M. Häringer, J. R. Binder, A. Hofmann, A. Smith, *Enabling Long-term Cycling Stability of $Na_3V_2(PO_4)_3$/C vs. Hard Carbon Full-cells*, **2023**.
[28] F. M. Maddar, D. Walker, T. W. Chamberlain, J. Compton, A. S. Menon, M. Copley, I. Hasa, *J. Mater. Chem. A* **2023**, *11*, 15778–15791.
[29] L. Mauler, F. Duffner, J. Leker, *Appl. Energy* **2021**, *286*, 116499.
[30] A. Kwade, W. Haselrieder, R. Leithoff, A. Modlinger, F. Dietrich, K. Droeder, *Nat. Energy* **2018**, *3*, 290–300.
[31] A. Jinasena, O. S. Burheim, A. H. Strømman, *Batteries* **2021**, *7*, 14.
[32] S. Michaelis, J. Schütrumpf, A. Kampker, H. Heimes, B. Dorn, S. Wennemar, A. Scheibe, S. Wolf, M. Smulka, B. Ingendoh et al., *Roadmap Battery Production Equipment 2030. Update 2023*, VDMA Verlag, **2023**.
[33] R. Diehm, H. Weinmann, J. Kumberg, M. Schmitt, J. Fleischer, P. Scharfer, W. Schabel, *Energy Technol.* **2020**, *8*, 1900137.
[34] T. Heckmann, J. C. Eser, A. Altvater, N. Streller, P. Scharfer, W. Schabel, *Energy Techn.* **2022//2023**, *11*, 2200859.
[35] F. Huttner, A. Marth, J. C. Eser, T. Heckmann, J. Mohacsi, J. K. Mayer, P. Scharfer, W. Schabel, A. Kwade, *Batteries & Supercaps* **2021**, *4*, 1499–1515.
[36] M. Müller, L. Pfaffmann, S. Jaiser, M. Baunach, V. Trouillet, F. Scheiba, P. Scharfer, W. Schabel, W. Bauer, *J. Power Sources* **2017**, *340*, 1–5.
[37] R. Morasch, J. Landesfeind, B. Suthar, H. A. Gasteiger, *J. Electrochem. Soc.* **2018**, *165*, A3459–A3467.
[38] F. Font, B. Protas, G. Richardson, J. M. Foster, *J. Power Sources* **2018**, *393*, 177–185.

© 2023 The Authors. Batteries & Supercaps published by Wiley-VCH GmbH

25666223, 2023, 11, Downloaded from https://chemistry-europe.onlinelibrary.wiley.com/doi/10.1002/batt.202300291 by Cochrane Germany, Wiley Online Library on [20/12/2023]. See the Terms and Conditions (https://onlinelibrary.wiley.com/terms-and-conditions) on Wiley Online Library for rules of use; OA articles are governed by the applicable Creative Commons License

[39] A. Altvater, T. Heckmann, J. C. Eser, S. Spiegel, P. Scharfer, W. Schabel, *Energy Technol.* **2022**, 2200785.
[40] M. Baunach, S. Jaiser, S. Schmelzle, H. Nirschl, P. Scharfer, W. Schabel, *Drying Technol.* **2016**, *34*, 462–473.
[41] B. Westphal, H. Bockholt, T. Gunther, W. Haselrieder, A. Kwade, *ECS Trans.* **2015**, *64*, 57–68.
[42] B. G. Westphal, A. Kwade, *J. Energy Storage* **2018**, *18*, 509–517.
[43] S. Jaiser, M. Müller, M. Baunach, W. Bauer, P. Scharfer, W. Schabel, *J. Power Sources* **2016**, *318*, 210–219.
[44] C.-C. Li, Y.-W. Wang, *J. Electrochem. Soc.* **2011**, *158*, A1361.
[45] Evangelos Tsotsas, Volker Gnielinski, Ernst-Ulrich Schlünder.
[46] E.-U. Schlünder, *Chem. Ing. Tech.* **1988**, *60*, 117–120.
[47] E.-U. Schlünder, *Drying Technol.* **2004**, *22*, 1517–1532.
[48] T. Metzger, E. Tsotsas, *Drying Technol.* **2005**, *23*, 1797–1809.
[49] R. Morasch, J. Landesfeind, B. Suthar, H. A. Gasteiger, *J. Electrochem. Soc.* **2018**, *165*, A3459-A3467.
[50] L. Schneider, J. Klemens, E. C. Herbst, M. Müller, P. Scharfer, W. Schabel, W. Bauer, H. Ehrenberg, *J. Electrochem. Soc.* **2022**, *169*, 100553.
[51] R. Diehm, J. Kumberg, C. Dörrer, M. Müller, W. Bauer, P. Scharfer, W. Schabel, *Energy Technol.* **2020**, *8*, 1901251.
[52] L. Pfaffmann, S. Jaiser, M. Müller, P. Scharfer, W. Schabel, W. Bauer, F. Scheiba, H. Ehrenberg, *J. Power Sources* **2017**, *363*, 460–469.
[53] T. Günther, D. Schreiner, A. Metkar, C. Meyer, A. Kwade, G. Reinhart, *Energy Technol.* **2020**, *8*, 1900026.
[54] A. Schilling, J. Schmitt, F. Dietrich, K. Dröder, *Energy Technol.* **2016**, *4*, 1502–1508.
[55] P. Gupta, İ. B. Üçel, P. Gudmundson, E. Olsson, *Exp. Mech.* **2020**, *60*, 847–860.
[56] S. Jaiser, N. Sanchez Salach, M. Baunach, P. Scharfer, W. Schabel, *Drying Technol.* **2017**, *35*, 1807–1817.
[57] T. Mezger, *Das Rheologie Handbuch. Für Anwender von Rotations- und Oszillations-Rheometern*, Vinzentz Network, Hannover, **2016**.
[58] S. Spiegel, A. Hoffmann, J. Klemens, P. Scharfer, W. Schabel, *Energy Technol.* **2022**, 2200684.
[59] W. B. Hawley, J. Li, *J. Energy Storage* **2019**, *25*, 100862.
[60] A. Hoffmann, S. Spiegel, T. Heckmann, P. Scharfer, W. Schabel, *J. Coat. Technol. Res.* **2022**, 1–12.
[61] P. M. Schweizer in *Premetered Coating Methods*, Springer, Cham, **2022**, pp. 511–593.
[62] J. Kumberg, M. Baunach, J. C. Eser, A. Altvater, P. Scharfer, W. Schabel, *Energy Technol.* **2021**, *9*, 2100013.
[63] J. Ruhland, T. Storz, F. Kößler, A. Ebel, J. Sawodny, J. Hillenbrand, P. Gönnheimer, L. Overbeck, G. Lanza, M. Hagen et al., Springer, Cham, **2022**, pp. 96–104.
[64] A. Benslimane, I. M. Bahlouli, K. Bekkour, D. Hammiche, *Appl. Clay Sci.* **2016**, *132*, 702–710.
[65] S. Jaiser, L. Funk, M. Baunach, P. Scharfer, W. Schabel, *J. Colloid Interface Sci.* **2017**, *494*, 22–31.
[66] J. Kumberg, M. Müller, R. Diehm, S. Spiegel, C. Wachsmann, W. Bauer, P. Scharfer, W. Schabel, *Energy Technol.* **2019**, *7*, 1900722.

Manuscript received: July 5, 2023
Revised manuscript received: August 25, 2023
Accepted manuscript online: August 28, 2023
Version of record online: September 8, 2023

© 2023 The Authors. Batteries & Supercaps published by Wiley-VCH GmbH

25666223, 2023, 11, Downloaded from https://chemistry-europe.onlinelibrary.wiley.com/doi/10.1002/batt.202300291 by Cochrane Germany, Wiley Online Library on [20/12/2023]. See the Terms and Conditions (https://onlinelibrary.wiley.com/terms-and-conditions) on Wiley Online Library for rules of use; OA articles are governed by the applicable Creative Commons License